

Syntheses, structures and properties of 5-azotetrazolyl salicylic acid and its lanthanide complexes†

Cite this: *Dalton Trans.*, 2014, **43**, 9090

Wen-Bin Chen,^a Zhi-Xin Li,^a Xin-Wei Yu,^a Meng Yang,^a Yan-Xuan Qiu,^a Wen Dong*^a and Ya-Qiu Sun*^b

Two hydrated 5-azotetrazolyl salicylic acid (H₃ASA) of [(H₃ASA)·H₂O] (**1**) and [(H₃ASA)·4H₂O] (**2**) and five H₃ASA based dinuclear Ln³⁺ complexes of {[Ln₂(H_{1.5}ASA)₄(H₂O)₈]·6H₂O} [Ln = Dy (**3**), Tb(**4**)], {[Gd₂(H_{1.5}ASA)₄(H₂O)₈]·5H₂O} (**5**), {[Sm₂(H_{1.5}ASA)₄(H₂O)₈]·6H₂O} (**6**) and {[Eu₄(H_{1.5}ASA)₈(H₂O)₁₆]·10H₂O} (**7**) have been synthesized and characterized by single crystal X-ray diffraction analysis. In **1** and **2**, the neutral H₃ASA molecules show a *trans*-enol-*E* isomer but display two different dihedral angles. Complexes **3–7** exhibit three types of dinuclear structures in which the anionic ligands show two *trans*-enol-*E/Z* isomers. The photochromic and photoluminescent properties of **1**, **3–7** and the magnetic properties for **3–7** were investigated.

Received 25th January 2014,
Accepted 15th March 2014

DOI: 10.1039/c4dt00278d

www.rsc.org/dalton

Introduction

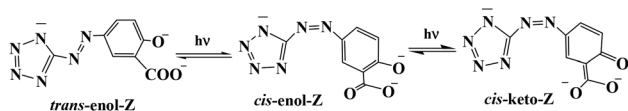
In the past few decades, a great deal of research has been carried out on lanthanide complex-based inorganic–organic hybrid materials due to their multifunctional, versatile and modulated properties.¹ It is believed that these types of hybrid materials can not only preserve or even improve the respective features of the components but also produce new properties depending on the synergy between the organic ligands and inorganic lanthanide ions. Because of the intrinsic abundant photoluminescent and magnetic properties of lanthanide ions, inorganic–organic hybrid lanthanide complexes can exhibit potential applications in the development of new lumi-

nescent and magnetic materials.² Currently, it is a particular challenge to assemble novel lanthanide complexes with different functional properties.³ An efficient approach for the generation of hybrids is to assemble appropriate organic ligands into lanthanide ion systems by coordinating bonding interactions. Because different ligands can control the structures and properties of the target molecules by different coordinating and bridging modes, choosing the right ligands is particularly important for the synthetic strategy. Triazole, tetrazole and salicylic acid have been proven to be desirable ligands due to their multicoordinating atoms and their own functional properties.⁴ Meanwhile, azo conjugated aromatic compounds are also desirable types of ligands because the azo linker is known to be an efficient electronic bridge, which prompts the creation of extended-conjugated systems, and such types of compounds can show a potential *trans* to *cis* photoisomerization property.⁵ Very recently, the pronounced bathochromic absorption and photochromism of 1,1'-azobis-1,2,3-triazole, 1,1'-azobis-tetrazole and 5,5'-azotetrazolate based complexes were reported.⁶ The H₃ASA, which contains azo, salicylic acid and tetrazole moieties, should be one of the especially desirable candidates because it can dissociate mono-, di- and trivalent anions, and each anion can not only give multiple coordinating and bridging modes, but also exhibit different *trans/cis*-enol/keto-*Z/E* isomers based on the photoisomerization reactions (Scheme 1). To the best of our knowledge, up to now there has not yet been a report concerning the structures, photochromic, photoluminescent and magnetic properties of well-defined single crystals of the H₃ASA based Ln³⁺ metallic complexes.⁷ Here, seven novel H₃ASA based compounds (**1–7**)

^aSchool of Chemistry and Chemical Engineering, Guangzhou Key Laboratory for Environmentally Functional Materials and Technology, Guangzhou University, Guangzhou, 510006, China. E-mail: dw320@aliyun.com

^bDepartment of Chemistry, Tianjin Normal University, Tianjin, 300383, China. E-mail: hxxyyq@mal.tjnu.edu.cn

† Electronic supplementary information (ESI) available: The atomic labeling diagrams of **4–7**; 3D supramolecular structures of **1–7**; photoisomerization of **1**; the temperature-dependent changes of UV-vis absorption spectra of aqueous solutions of **1**; TD-DFT calculations for the absorption spectra of the alkaline aqueous solution of **1**; the color changes of **4–7** before and after 365 nm UV irradiation; luminescent spectra of **1** and **5–7**; X-ray powder diffraction patterns for **3–7**; the plots of $\chi_M T$ versus T for **4–7**; M versus H plots in the field range 0–40 000 (70 000) Oe for **3–5**; M versus H/T plots in the field range 0–70 000 Oe for **4**; temperature-dependence of the in-phase (χ'') and out-of-phase (χ''') of ac susceptibility of **3** at 250–1500 Hz; the $1/\chi_M$ versus T plot in the range from 300 to 2 K for **5** and CIF files. CCDC 922441 for **1**, 946733 for **2**, 922442 for **3**, 922443 for **4**, 922444 for **5**, 922445 for **6**, 922446 for **7**. For ESI and crystallographic data in CIF or other electronic format see DOI: 10.1039/c4dt00278d



Scheme 1 The photoisomerization reaction of the ASA^{3-} anion.

were synthesized and their crystal structures, photochromism, photoluminescence and magnetism were investigated and discussed.

Experimental

Materials and physical measurements

All commercial reagents and solvents were used without further purification unless otherwise stated. IR spectra were recorded as pressed KBr pellets on a Bruker Tensor 27 spectrophotometer. Elemental analyses were carried out using a Perkin-Elmer analyzer model 240. UV-vis absorption spectra of **1** in aqueous solution were collected on a U-1800 Ultraviolet-Visible Spectrophotometer. The solid-state diffuse reflectance spectra were measured on a Hitachi UV-2501PC spectrophotometer equipped with an integrating sphere attachment and against a BaSO_4 plate as the standard. Luminescence spectra were recorded with an F-4500 fluorescence spectrophotometer. Fluorescent imaging experiments for solid samples were conducted with a Nikon 55i Fluorescent Microscope. The magnetic measurements of the sample of 3–7 were carried out using a SQUID magnetometer in the temperature range of 2–300 K at a constant magnetic field (1000 Oe). AC data were collected in the range 2–5.5 K with an applied alternating field of 3.5 Oe at different frequencies in the range 0–1500 Hz.

X-Ray crystallography and data collection

The crystals were filtered from the solution and immediately coated with hydrocarbon oil on the microscope slide. Suitable crystals were mounted on glass fibers with silicone grease and placed in a Bruker Smart APEX(II) area detector using graphite monochromated $\text{Mo-K}\alpha$ radiation ($\lambda = 0.71073 \text{ \AA}$) at 173(2)/298(2) K. The structures were solved by direct methods and successive Fourier difference syntheses (SHELXS-97) and refined by full-matrix least-squares procedure on F^2 with anisotropic thermal parameters for all non-hydrogen atoms (SHELXL-97). Hydrogen atoms in the azotetrazolyl were added by electron density peak and other hydrogen atoms including water hydrogen atoms were added theoretically and were riding on their parent atoms. CCDC 922441 for **1**, 946733 for **2**, 922442 for **3**, 922443 for **4**, 922444 for **5**, 922445 for **6**, 922446 for **7**.†

Quantum calculations

All the quantum-chemical calculations were performed with the Gaussian 09 suite using the time dependent density functional theory (TD-DFT) method at the B3LYP/6-31+G(d,p) level based on the crystal structures obtained in this work. Orbital

composition analysis was performed with the Hisfeld method using the program Multiwfn 2.5.⁸

Syntheses of $[(\text{H}_3\text{ATSA})\cdot\text{H}_2\text{O}]$ (**1**) and $[(\text{H}_3\text{ASA})\cdot 4\text{H}_2\text{O}]$ (**2**)

5-Azotetrazolyl salicylic acid was synthesized according to the method reported in ref. 9: 5-amino-1H-tetrazole (2.06 g, 0.02 mol) was dissolved in 50 mL of distilled water, 3 mL of concentrated hydrochloric acid was added. The reaction solution was stirred, cooled and kept at -5 to 0°C in an ice bath (ice and sodium chloride) and diazotized by the slow addition of a solution of sodium nitrite (0.02 mol, 1.38 g) in water (20 mL), followed by stirring for 30 min at -5 to 0°C . Then a solution of salicylic acid (0.02 mol, 2.76 g) in ethanol (20 mL) was slowly added to the solution of the diazonium salt at 0 – 5°C . The resulting mixture was stirred for 12 h and then the yellow precipitate was filtered and washed with water (yield: 73.2%). The yellow crystals of **1** and red crystals of **2** were obtained after recrystallization in acid solution with a pH of about 5. FT-IR (KBr, cm^{-1}): 3241m, 1659s, 1494s, 1445s, 1186s, 760m, 696m for **1**. Anal. Calcd for **1** of $\text{C}_8\text{H}_8\text{N}_6\text{O}_4$ (%): C, 38.07; H, 3.17; N, 33.31. Found(%): C, 38.11; H, 3.26; N, 33.35. FT-IR (KBr, cm^{-1}): 3456m, 3236s, 1661s, 1483s, 1444s, 1294s, 1156s, 891s, 756s, 695s, 533m for **2**. Anal. Calcd for **2** of $\text{C}_8\text{H}_{14}\text{N}_6\text{O}_7$ (%): C, 31.35; H, 4.57; N, 27.43. Found(%): C, 31.25; H, 4.78; N, 27.38.

Syntheses of 3–6

10 mL aqueous solution of $\text{MCl}_3\cdot 6\text{H}_2\text{O}$ (0.01 mmol) was added to a solution of 5-azotetrazolyl salicylic acid (0.0504 g, 0.2 mmol) in 10 mL of water and 10 mL of ethanol and stirred for 5 min, then a drop of dilute $\text{NH}_3\cdot\text{H}_2\text{O}$ (2 mol L^{-1}) was added to adjust the pH to about 5. The resulting mixture was filtered and block crystals were obtained by slow evaporation of the filtrate after several days, which were then washed with ethanol to give a 36.5% yield of **3** (based on Dy^{3+}), 28.9% yield of **4** (based on Tb^{3+}), 28.5% yield of **5** (based on Gd^{3+}) and 33.2% yield of **6** (based on Sm^{3+}). Anal. Calcd for **3** of $\text{C}_{32}\text{H}_{46}\text{N}_{24}\text{O}_{26}\text{Dy}_2$ (%): C, 25.47; H, 3.05; N, 22.28. Found(%): C, 25.49; H, 3.09; N, 22.32. FT-IR (KBr, cm^{-1}): 3196m, 1627m, 1580s, 1443s, 1175m, 837w, 683m, 563w. Anal. Calcd for **4** of $\text{C}_{32}\text{H}_{46}\text{N}_{24}\text{O}_{26}\text{Tb}_2$ (%): C, 25.59; H, 3.07; N, 22.39. Found(%): C, 25.63; H, 3.13; N, 22.45. FT-IR (KBr, cm^{-1}): 3306m, 1635m, 1558s, 1391s, 1246m, 1149m, 756m, 671m. Anal. Calcd for **5** of $\text{C}_{32}\text{H}_{42}\text{N}_{24}\text{O}_{26}\text{Gd}_2$ (%): C, 25.71; H, 2.81; N, 22.50. Found(%): C, 25.76; H, 2.84; N, 22.56. FT-IR (KBr, cm^{-1}): 3234m, 1628m, 1582s, 1387s, 1170m, 844w, 681m, 561w. Anal. Calcd for **6** of $\text{C}_{32}\text{H}_{46}\text{N}_{24}\text{O}_{26}\text{Sm}_2$ (%): C, 25.88; H, 3.10; N, 22.65. Found(%): C, 25.60; H, 3.21; N, 22.69. FT-IR (KBr, cm^{-1}): 3151s, 1623m, 1593s, 1441s, 1173m, 840w, 684m.

Syntheses of 7

10 mL aqueous solution of $\text{EuCl}_3\cdot 6\text{H}_2\text{O}$ (0.0366 g, 0.01 mmol) was added to a solution of 5-azotetrazolyl salicylic acid (0.0756 g, 0.3 mmol) in 10 mL of water and 10 mL of ethanol and stirred for 5 min and a drop of dilute $\text{NH}_3\cdot\text{H}_2\text{O}$ (2 mol L^{-1}) was added to adjust the pH to about 5. The resulting mixture

was filtered and block crystals were obtained by slow evaporation of the filtrate after several days and washed with ethanol. Yield: 31.6% (based on Eu^{3+}). Anal. Calcd for 7 of $\text{C}_{64}\text{H}_{92}\text{N}_{48}\text{O}_{52}\text{Eu}_4$ (%): C, 25.83; H, 3.09; N, 22.60. Found(%): C, 25.86; H, 3.21; N, 22.65. FT-IR (KBr, cm^{-1}): 3396m, 3225m, 1627m, 1580s, 1441s, 1170s, 837m, 681m, 561m.

Results and discussion

Crystal structures of 1–7

Table 1 gives the crystallographic data for compounds 1–7. The atomic labeling diagrams for 1 and 2 are shown in Fig. 1a,b, respectively. The crystals of 1 and 2 are yellow and red, respectively. 1 and 2 show two different space groups in which each unit cell contains a fundamental H_3ASA molecule and two different lattice water molecules. In 1 and 2, the neutral H_3ASA molecules show a *trans-enol-E* isomer with the bond length for C2–O3 (phenol) being 1.354(3) Å for 1 and 1.341(4) Å for 2. The dihedral angles between the tetrazole and phenyl ring of H_3ASA are 0.62° in 1 and 39.1° in 2, which display a coplanar and very twisted structure, respectively. The yellow colour of 1 and red of 2 should originate from the differences in dihedral angles. The O–H...O and O–H...N hydrogen bonding and π – π stacking interactions between the tetrazole and phenyl rings are responsible for the stabilization of the 3D supramolecular structure (Fig. S2, ESI†). The atomic labeling diagram of 3 is depicted in Fig. 1c and the atomic labeling diagrams of 4–7 are shown in Fig. S3 ESI.† Complexes 3 and 4 are isostructural molecules in which each Dy^{3+} or Tb^{3+} ion coordinates to four carboxylate oxygen atoms from three ligands and four water molecules to give an eight-coordinated square antiprism. In complex 5, each Gd^{3+} ion shows a square antiprism environment surrounded by eight oxygen atoms from four carboxylate oxygen atoms of three ligands and four water molecules. Each Sm^{3+} ion shows a distorted tricapped trigonal prismatic environment surrounded by nine oxygen atoms from four carboxylate oxygen atoms of three ligands and five water molecules in complex 6. However, there are two μ_2 bridging water molecules in 6 (Fig. S3c, ESI†). In 7, there are two different coordinating environments for Eu^{3+} ions in which an Eu^{3+} ion shows an eight-coordinated environment that is similar to the Dy^{3+} ion in 3 and another Eu^{3+} ion is nine-coordinated with a tricapped trigonal prismatic structure. In 3–7, the H_2ASA^- and HASA^{2-} anions show *trans-enol-E* and *trans-enol-Z* isomers, respectively. The H_2ASA^- anion acts as a chelate ligand with two carboxylate oxygen atoms coordinating to a Ln^{3+} ion and each HASA^{2-} anion acts as a μ_2 bridging ligand with two carboxylate oxygen atoms linking two Ln^{3+} ions to give a dinuclear complex. The $\text{Ln}^{3+}\cdots\text{Ln}^{3+}$ distances are 4.88, 4.85, 5.13, 4.23 and 4.93(5.32) Å for 3–7, respectively. The H_2ASA^- and HASA^{2-} anionic ligands are approximately coplanar because the dihedral angles between the tetrazole and phenyl ring are 1.30 and 7.62° for 3, 1.53 and 7.88° for 4, 1.35 and 3.62° for 5, 10.30 and 11.20° for 6, and 1.93 and 5.32° for 7. In complexes 3–7, the π – π stacking between the tetrazole and phenyl aromatic

Table 1 The crystal data and data collection parameters for 1–7

	1	2	3	4	5	6	7
Formula	$\text{C}_8\text{H}_8\text{N}_6\text{O}_4$	$\text{C}_8\text{H}_8\text{N}_6\text{O}_7$	$\text{C}_{32}\text{H}_{46}\text{Dy}_2\text{N}_{24}\text{O}_{26}$	$\text{C}_{32}\text{H}_{46}\text{N}_2\text{O}_{26}\text{Tb}_2$	$\text{C}_{32}\text{H}_{46}\text{Gd}_2\text{N}_{24}\text{O}_{26}$	$\text{C}_{32}\text{H}_{46}\text{N}_2\text{O}_{26}\text{Sm}_2$	$\text{C}_{64}\text{H}_{92}\text{Eu}_4\text{N}_{48}\text{O}_{52}$
Formula weight	252.20	306.25	1507.93	1500.79	1497.43	1483.65	2973.74
Crystal system	Monoclinic	Monoclinic	Triclinic	Triclinic	Triclinic	Triclinic	Triclinic
Space group	$P2_1/n$	$C2/c$	$P1$	$P1$	$P1$	$P1$	$P1$
$a/\text{\AA}$	3.9726(2)	27.104(10)	9.6459(14)	9.6491(13)	9.76740(10)	9.6865(12)	11.8805(2)
$b/\text{\AA}$	10.6370(6)	3.8044(13)	11.9523(18)	11.9680(17)	11.8082(2)	11.7997(14)	14.6591(3)
$c/\text{\AA}$	24.5982(13)	27.047(9)	12.8750(19)	12.9137(18)	12.5681(2)	13.1112(16)	16.4889(3)
$a/\text{\AA}^\circ$	90.00	90.00	110.424(2)	110.617(2)	109.4910(10)	111.997(2)	99.9840(10)
$\beta/\text{\AA}^\circ$	91.158(4)	101.58(2)	94.582(2)	94.603(2)	94.4350(10)	95.839(2)	95.9560(10)
$\gamma/\text{\AA}^\circ$	90.00	90.00	105.450(2)	105.596(2)	104.6290(10)	104.792(2)	110.3260(10)
Volume/ \AA^3	1039.22(10)	2732.2(17)	1316.0(3)	1318.8(3)	1301.27(4)	1310.5(3)	2609.93(9)
Z	4	8	1	1	1	1	1
$\rho_{\text{calc}}/\text{mg mm}^{-3}$	1.612	1.489	1.903	1.890	1.911	1.880	1.892
μ/mm^{-1}	0.133	0.131	2.926	2.769	2.637	2.328	2.491
$F(000)$	520.0	1280.0	746.0	744.0	742.0	738.0	1480.0
Reflections collected	6711	10 622	11 004	11 019	19 222	10 980	41 058
Independent	1835 [$R(\text{int}) = 0.0454$]	3135 [$R(\text{int}) = 0.0454$]	5800 [$R(\text{int}) = 0.0186$]	5783 [$R(\text{int}) = 0.0166$]	5122 [$R(\text{int}) = 0.0255$]	5770 [$R(\text{int}) = 0.0182$]	12 090 [$R(\text{int}) = 0.0212$]
Goodness-of-fit on F^2	1.090	1.075	1.092	1.157	1.039	1.194	1.036
Final R indexes	$R_1 = 0.0561^a$ $wR_2 = 0.1563^b$	$R_1 = 0.0705$ $wR_2 = 0.2087$	$R_1 = 0.0236$ $wR_2 = 0.0538$	$R_1 = 0.0211$ $wR_2 = 0.0567$	$R_1 = 0.0322$ $wR_2 = 0.0721$	$R_1 = 0.0236$ $wR_2 = 0.0667$	$R_1 = 0.0244$ $wR_2 = 0.0594$
Final R indexes	$R_1 = 0.0710$ $wR_2 = 0.1663$	$R_1 = 0.1192$ $wR_2 = 0.2402$	$R_1 = 0.0238$ $wR_2 = 0.0568$	$R_1 = 0.0267$ $wR_2 = 0.0609$	$R_1 = 0.0367$ $wR_2 = 0.0784$	$R_1 = 0.0282$ $wR_2 = 0.0748$	$R_1 = 0.0292$ $wR_2 = 0.0621$
[all data]							

$$^a R = \sum ||F_o| - |F_c|| / \sum |F_o|, \quad ^b wR_2 = [\sum w(F_o^2 - F_c^2)^2 / \sum w(F_o^2)]^{1/2}.$$

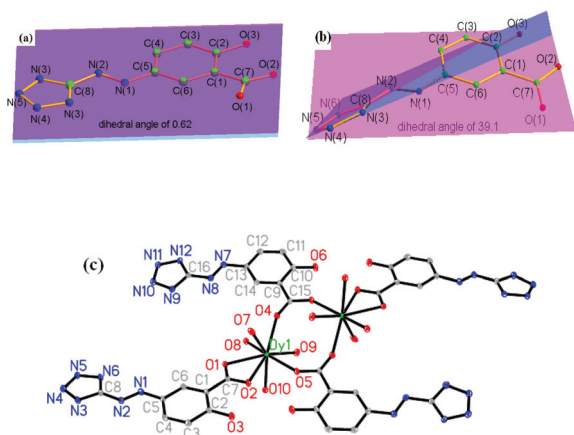


Fig. 1 The atomic labeling diagrams: (a) for 1, (b) for 2, (c) for 3. All H atoms and lattice water molecules have been omitted for clarity.

rings and the two O–H...O and O–H...N hydrogen bonding interactions link the complex units and lattice water molecules to give a 3D supramolecular packing structure (Fig. S4, ESI†).

The pH-dependent UV-vis spectra and photochromism of aqueous solution of 1

Fig. 2a gives the pH-dependent UV-vis spectra of the aqueous solution of 1 with a concentration of 5×10^{-5} mol dm⁻³. The pH of the aqueous solution of 1 (5×10^{-5} mol dm⁻³) is 4.55. When the pH increases from 4.55 to 10.21 by titration with

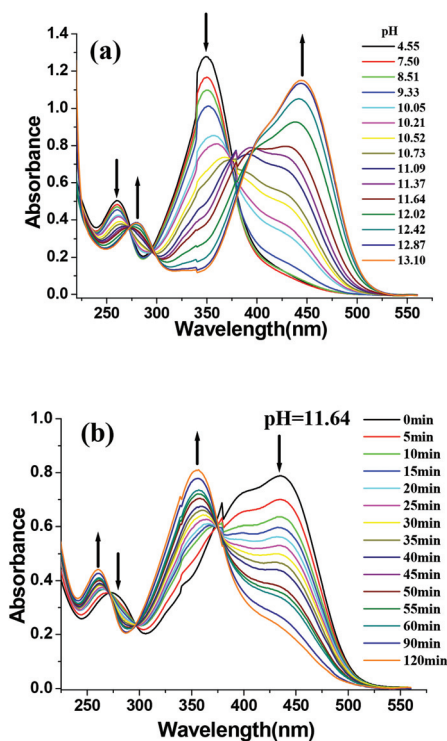


Fig. 2 (a) The pH-dependent UV-vis spectral changes of the aqueous solutions of 1. (b) The UV-vis spectral changes of 1 in alkaline aqueous solution with a pH of 11.64 under 365 nm UV irradiation.

2 mol L⁻³ NaOH aqueous solution, the solutions show two clearly intense absorption peaks at 260 and 355 nm accompanied by a decrease in intensity and an unresolved weak shoulder peak around 430 nm. When the pH increases from 10.21 to 11.64, an added new red-shifted maximum absorption peak around 445 nm appears with an increase in intensity. When the pH increases from 11.64–13.10, the solution exhibits two maximum absorption peaks around 276 and 445 nm and a weak shoulder peak around 410 nm. The absorption peaks for the aqueous solution of 1 at a pH scale of 4.55–13.10 should originate from the intrinsic chromophoric salicylic and tetrazolate π or azo n electronic excitation of the *trans*-enol isomers of H₃ASA or its anions. Fig. 2b gives the photochromic properties for the alkaline aqueous solution of 1 with a concentration of 5×10^{-5} mol dm⁻³ and a pH of 11.64 under 365 nm UV light irradiation at room temperature. Upon irradiation of the aqueous solution for 5 minutes with 365 nm UV light, two absorption peaks around 276 and 445 nm decrease in intensity and two new absorption peaks at around 260 and 355 nm are noted, also four regions with three isosbestic points at 270, 297 and 375 nm can be distinguished. When the UV light irradiation continuously increases for 25 minutes, the absorption intensity at the 355 nm peak largely increases. When the time of UV light irradiation increases for 60 minutes, the original two absorption peaks at 276 and 445 nm become unresolved. The phenomenon of the maximum absorption peak transfer from 445 to 355 nm should originate from the *trans*-enol to *cis*-enol photoisomerization reaction of the ASA³⁻ anion (Scheme 1).^{6c} Moreover, the photochromism of the aqueous solution of 1 is in accordance with the first-order kinetics (Fig. S5, ESI†), and the photochromism rate constant is about 2.824×10^{-2} min⁻¹.^{6a} The temperature-dependent changes of the UV-vis absorption spectra of the alkaline aqueous solutions of 1 with a concentration of 5×10^{-5} mol dm⁻³ and pH of 11.64 in the temperature range of 32–100 °C are given in Fig. S6, ESI.† When the temperature of the aqueous solutions of 1 increases from 32 to 100 °C, the three absorption peaks around 280, 400 and 445 nm decrease in intensity and two new absorption peaks at around 260 and 355 nm are noted, also four regions with three isosbestic points at 270, 297 and 375 nm could be distinguished. The thermo-chromic properties of the aqueous solutions of 1 are very similar to the characteristics of photochromism and should also be assigned to the *trans*-enol to *cis*-enol isomeric reaction of the ASA³⁻ anion. For the TD-DFT calculations of the absorption peaks of the alkaline aqueous solution of 1 and the photoisomerization reaction see the ESI (Fig. S7, ESI†).

The photochromic properties of crystal powder samples of 1 and 3

Fig. 3 gives the color changes and the corresponding diffuse reflectance spectra of the crystal powder samples of 1 and 3 after 365 nm UV light irradiation at room temperature. From the diagrams, the two crystal powder samples change to dark brown from the original bright yellow for 1 and orange for 3 after irradiation for 30 min. Before light irradiation, the crystal

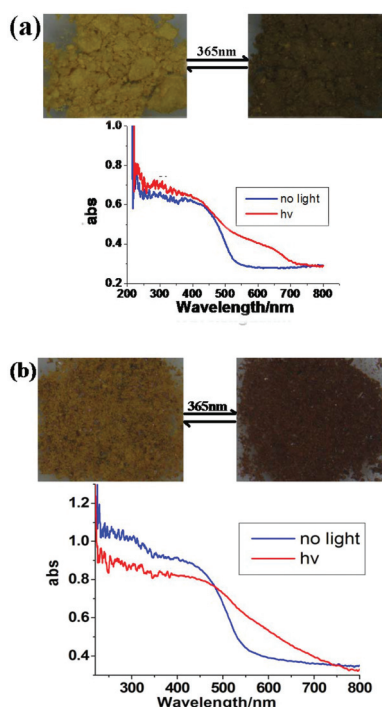


Fig. 3 (a), (b) The color and corresponding diffuse reflectance spectra of the crystal powder samples of **1** and **3** before and after 365 nm UV light irradiation, respectively.

powder samples of **1** and **3** display two distinguishable absorption peaks centered around 330 nm and 450 nm. After light irradiation, the samples show a new red shift peak at around 600 nm. The absorption peak around 330 nm and 450 nm can be attributed to the intrinsic π electronic transitions from the chromophoric tetrazolate, azo and salicylic groups. The larger red shift peak around 600 nm may be attributed to the keto isomer from the photoisomeric reaction.¹⁰ The crystal powder samples of **4**–**7** show similar photochromic properties to **3** (Fig. S8, ESI[†]).

Luminescence of the solid samples of **1**, **3**–**7**

The photoluminescent spectra of the solid samples of **1**, **3**–**7** are depicted in Fig. 4 and Fig. S9, ESI[†]. Under 340 nm UV light excitation, the solid phase of **1** exhibits a maximum emissive peak around 460 nm and a shoulder peak around 370 nm (Fig. 4a). The solid sample of **1** shows a blue image when observed by a fluorescent microscope under UV light excitation (Fig. 4a, insert). Both solid samples of **3** and **4** exhibit Dy³⁺ and Tb³⁺ ionic characteristic fluorescent emissive peaks under 340 nm UV light excitation, respectively (Fig. 4b). **3** exhibits the 480 and 571 nm characteristic emissive peaks of the Dy³⁺ ion, and the 457 and 529 nm characteristic peaks of the H₂ASA⁻ and HASA²⁻ anionic ligands. The 480 and 571 nm peaks should correspond to the ⁴F_{9/2}–⁶H_{15/2}, ⁴F_{9/2}–⁶H_{13/2} transitions, respectively. The 457 and 529 nm maximum emissive peaks should originate from the π electronic radiative relaxation of the anionic ligands. **4** displays four characteristic emissive

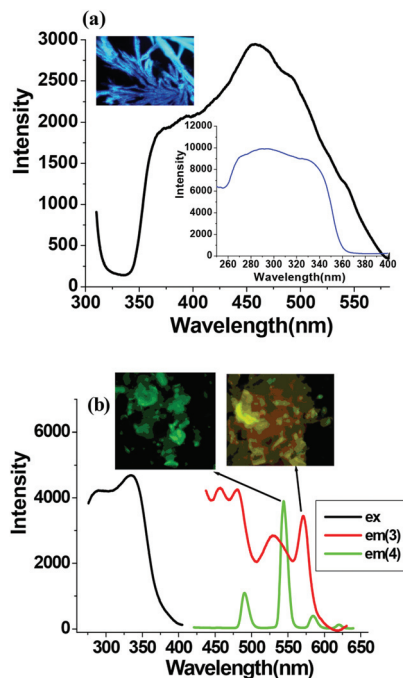


Fig. 4 (a) The emission spectra of **1**. (b) Excitation and emission spectra of **3** and **4**. Inset is the photoluminescent image of the solid sample of **1**, **3**, **4** taken with a fluorescent microscope.

peaks of the Tb³⁺ ion around 491, 543, 584 and 620 nm, which correspond to the ⁵D₄–⁷F₆, ⁵D₄–⁷F₅, ⁵D₄–⁷F₄, ⁵D₄–⁷F₃ transitions, respectively. The two solid samples of **3** and **4** display yellow-green images and green images when observed by a fluorescent microscope under UV light excitation, respectively (Fig. 4b, insert). However, the solid samples of **5**–**7** only display two fluorescent emissive peaks, around 460 and 540 nm, that come from the anionic ligands, with the characteristic fluorescent emissive peaks of Sm³⁺ and Eu³⁺ ions not being observed (Fig. S9, ESI[†]). Based on the above photoluminescent spectra of **1**, **3**–**7**, a selective antenna effect of the H₃ASA ligand for inducing Dy³⁺ and Tb³⁺ ion photoluminescence was found.

Magnetic properties of **3**–**7**

In order to probe the magnetic behaviour of **3**–**7**, the temperature dependence of the magnetic susceptibilities of **3**–**7** have been measured for microcrystalline samples over the temperature range 2–300 K under an applied direct current (dc) magnetic field of 1000 Oe. The plots of $\chi_M T$ versus T for **3**–**7**, where χ_M is the molar magnetic susceptibility, are shown in Fig. 5 and Fig. S10, ESI[†]. As shown in Fig. 5a, the observed $\chi_M T$ value for **3** at 300 K is 28.87 cm³ K mol⁻¹, which is in agreement with the theoretical value of 28.34 cm³ K mol⁻¹ for two non-interacting Dy³⁺ ions (⁶H_{15/2}, $S = 5/2$, $L = 5$, $g = 4/3$, $\chi T = 14.17$ cm³ K mol⁻¹). Upon decreasing the temperature, $\chi_M T$ gradually decreases to reach 23.40 cm³ K mol⁻¹ at 4.5 K. The decreasing values of $\chi_M T$ is most likely due to depopulation of the Stark sublevels in Dy³⁺ systems. Finally, below 4.5 K a sharp increase can be observed and the $\chi_M T$ reaches a maximum value of 25.60 cm³ K mol⁻¹ at 2 K. Such an increase

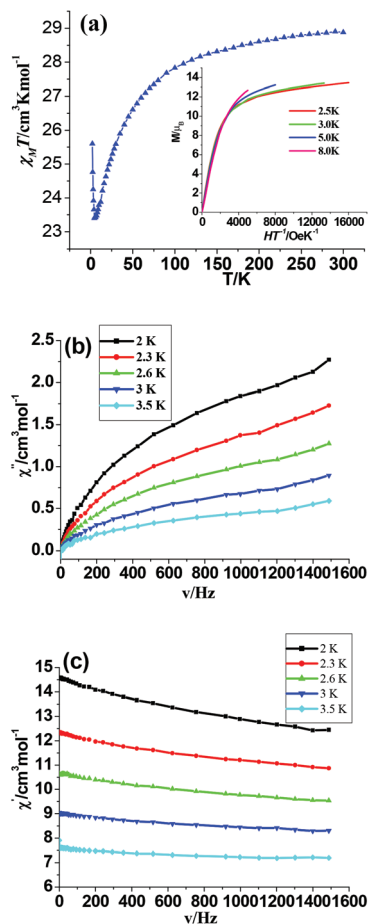


Fig. 5 (a) The plot of $\chi_M T$ versus T for **3** in the magnetic field of 1000 Oe at 2–300 K. Insert is the plot of M versus H/T in the field range 0–40 000 Oe; (b) (c) frequency-dependence of the in-phase (χ') and out-of-phase (χ'') of ac susceptibility of **3** at 2 K–3.5 K.

can be attributed to intramolecular ferromagnetic interactions between the Dy^{3+} ions.^{11,12} The magnetization (M) of **3** that was collected from a zero dc field to 40 kOe below 8 K is shown in Fig. S11, ESI†. The magnetization of **3** shows a relatively rapid increase below 10 kOe and a slow linear increase without complete saturation up to 40 kOe. The magnetization reaches a maximum value of $13.5\mu_B$ at 2.5 K and 40 kOe. This value is lower than the expected saturation value for two non-interacting Dy^{3+} ions [$g_J \times J = 4/3 \times 15/2 = 10\mu_B$ per Dy^{3+}], which is likely due to crystal-field effects and the low-lying excited states. The M versus H/T plot is given in the insert of Fig. 5a. The lack of a superimposition on a single master curve as expected for an isotropic system with a well-defined ground state and the lower magnetization values for **3** suggests the presence of low-lying excited states or/and significant magnetic anisotropy.¹¹ The alternating current (ac) magnetic susceptibility for **3** was performed in a zero-dc field as a function of the ac frequency between 0.1 and 1500 Hz in the temperature range 2–3.5 K (Fig. 5b,c). The in-phase (χ') and out-of-phase (χ'') signals show obvious frequency dependence at low temperature, but no peak was observed (Fig. S12, ESI†). The energy

barriers and relaxation times were approximated using a method recently employed by Bartolome *et al.*¹³ based on the following equation:

$$\ln\left(\frac{\chi''}{\chi'}\right) = \ln(\omega\tau) + E_a/k_B T$$

The calculated energy barrier of **3** was found to be 3.75 K whereas the relaxation time is 5.76×10^{-5} s (Fig. S13, ESI†). This behavior is consistent with the behavior of a single molecule magnet and the values of the energy barrier and relaxation time are comparable with that observed in other $\text{Dy}(\text{III})$ -based SMMs.^{12,14}

The plot $\chi_M T$ versus T for **4** is depicted in Fig. S10, ESI†. The $\chi_M T$ value of $24.09 \text{ cm}^3 \text{ K mol}^{-1}$ at 300 K is in good agreement with the expected value of $23.63 \text{ cm}^3 \text{ K mol}^{-1}$ for two non-interacting Tb^{3+} ions (7F_6 , $S = 3$, $L = 3$, $g = 3/2$). Upon cooling to 12 K, the $\chi_M T$ of the product gradually decreases to $21.47 \text{ cm}^3 \text{ K mol}^{-1}$, which is most likely due to the depopulation of the Stark sublevels in the Tb^{3+} systems. Then the $\chi_M T$ of the product increases to $27.85 \text{ cm}^3 \text{ K mol}^{-1}$ at 2 K, which is probably due to the presence of an intramolecular ferromagnetic interaction between the Tb^{3+} ions. The M versus H plots for **4** in the field range 0–70 000 Oe below 8 K are shown in Fig. S14, ESI†. The magnetization measurement for **4** also shows a relatively rapid increase below 10 kOe and a slow linear increase without complete saturation up to 70 kOe. The maximum magnetization of $11.5\mu_B$ at 70 kOe at 2.5 K is lower than the expected saturation value for two non-interacting Tb^{3+} ions [$g_J \times J = 3/2 \times 6 = 9\mu_B$ per Tb^{3+}]. The M versus H/T plots for **4** shows no superimposition on a single master curve (Fig. S15, ESI†), which suggests the presence of low-lying excited states or/and significant magnetic anisotropy. The magnetic susceptibility studies of **5–7** were plotted as $\chi_M T$ versus T in Fig. S9, ESI†. The observed $\chi_M T$ values at 300 K are 12.27, 0.19 and $6.78 \text{ cm}^3 \text{ K mol}^{-1}$ for **5–7**, respectively. The theoretical calculated $\chi_M T$ values for two non-interacting Gd^{3+} (${}^8S_{7/2}$, $S = 7/2$, $L = 0$, $g = 2$) ions are $15.76 \text{ cm}^3 \text{ K mol}^{-1}$. Upon decreasing the temperature, $\chi_M T$ gradually decreases to reach $9.06 \text{ cm}^3 \text{ K mol}^{-1}$ at 2 K, which indicates antiferromagnetic interactions between Gd^{3+} ions. The $1/\chi_M$ versus T plot in the range from 300 to 2 K obeys the Curie–Weiss law ($\chi_M = C/(T - \theta)$) with a Weiss constant θ of -7.13 K (Fig. S16, ESI†). The negative Weiss constant further confirms an intramolecular antiferromagnetic interaction between adjacent Gd^{3+} ions. The field dependence of the magnetisation below 8 K reveals a relatively rapid increase of the magnetisation below 10 kOe and then a very slow linear increase without complete saturation up to 70 kOe (Fig. S17, ESI†). The maximum magnetization of $7.83\mu_B$ at 70 kOe is lower than the expected saturation value for two non-interacting Gd^{3+} ions [$g_J \times J = 2 \times 7/2 = 7\mu_B$ per Gd^{3+}]. For **6**, the theoretical calculated $\chi_M T$ values for two non-interacting Sm^{3+} (${}^6H_{5/2}$, $S = 5/2$, $L = 5$, $g = 2/7$) ions are $0.18 \text{ cm}^3 \text{ K mol}^{-1}$, which is in agreement with the observed value. However, the magnetic properties of the Eu^{3+} ions in **7** are difficult to interpret even at room temperature due to the presence of thermally populated excited states.

Conclusions

In summary, a novel organic functional ligand of H₃ASA with two hydrated crystals that are yellow (1) and red (2) in color, and its five lanthanide complexes (3–7) were synthesized and reported for the first time. The solids of 1, 3–7 display photochromic properties and the *trans*-enol to *cis*-enol transition for the ASA³⁻ anion is demonstrated by TD-DFT calculations. The photoluminescence of the solids of 1, 3–7 were reported and a selective antenna effect of the H₃ASA ligand for inducing Dy³⁺ and Tb³⁺ ionic photoluminescence was found. The magnetic properties of 3–7 were investigated and the SMM behavior of 3 was demonstrated. This work demonstrates that H₃ASA based lanthanide complexes show photochromic, photoluminescent and magnetic properties and are promising novel functional materials that may be suitable for applications in optical and magnetic devices.

Acknowledgements

This work was supported by the National Natural Science Foundation of China (no. 21271052), the Science and Technology Program Foundation of Guangzhou (no. 2013J4100016) and the Program Foundation of the second batch of innovation teams of Guangzhou Bureau of Education (13C04).

Notes and references

- (a) J. Feng and H. J. Zhang, *Chem. Soc. Rev.*, 2013, **42**, 387; (b) Y. Cui, Y. Yue, G. Qian and B. Chen, *Chem. Rev.*, 2012, **112**, 1126; (c) L. D. Carlos, R. A. S. Ferreira, V. Z. Bermudez, B. Julián-López and P. Escribano, *Chem. Soc. Rev.*, 2011, **40**, 536; (d) A. Dolbecq, E. Dumas, C. R. Mayer and P. Mialane, *Chem. Rev.*, 2010, **110**, 6009; (e) C. Sanchez, B. Julian, P. Belleville and M. Popall, *J. Mater. Chem.*, 2005, **15**, 3559; (f) K. Binnemans, *Chem. Rev.*, 2009, **109**, 4283; (g) Z. H. Zhang, T.-A. Okamura, Y. Hasegawa, H. Kawaguchi, L. Y. Kong, W. Y. Sun and N. Ueyama, *Inorg. Chem.*, 2005, **44**, 6219.
- (a) E. DeOliveira, C. R. Neri, O. A. Serra and A. G. S. Prado, *Chem. Mater.*, 2007, **19**, 5437; (b) J. D. Rinehart, M. Fang, W. J. Evans and J. R. Long, *Nat. Chem.*, 2011, **3**, 538; (c) H. B. Kagan, *Chem. Rev.*, 2002, **102**, 1805; (d) R. Sessoli and A. K. Powell, *Coord. Chem. Rev.*, 2009, **253**, 2328; (e) S. V. Eliseeva and J.-C. G. Bünzli, *Chem. Soc. Rev.*, 2010, **39**, 189; (f) J. Rocha, L. D. Carlos, F. A. A. Paz and D. Ananias, *Chem. Soc. Rev.*, 2011, **40**, 926.
- (a) P. Lodahl, A. V. Driel, I. Nikolaev, A. Irman, K. Overgaag, D. Vanmaekelbergh and W. Vos, *Nature*, 2004, **430**, 654; (b) X.-Y. Chen, G. S. Goff, W. C. Ewing, B. L. Scott and W. Runde, *Inorg. Chem.*, 2012, **51**, 13254; (c) G. Wang, Q. Peng and Y. Li, *Acc. Chem. Res.*, 2011, **44**, 322; (d) A. de Bettencourt-Dias, P. S. Barber and S. Bauer, *J. Am. Chem. Soc.*, 2012, **134**, 6987; (e) E. Pershagen, J. Nordholm and K. E. Borbas, *J. Am. Chem. Soc.*, 2012, **134**, 9832; (f) P. P. Lima, M. M. Nolasco, F. A. A. Paz, R. A. S. Ferreira, R. L. Longo, O. L. Malta and L. D. Carlos, *Chem. Mater.*, 2013, **25**, 586.
- (a) I. P. Pozdnyakova, A. Pigliucci, N. Tkachenko, V. F. Plyusnin, E. Vauthey and H. Lemmetyinen, *J. Phys. Org. Chem.*, 2009, **22**, 449; (b) H.-C. Lüdemann, F. Hillenkamp and R. W. Redmond, *J. Phys. Chem. A*, 2000, **104**, 3884; (c) N. Matyasovszky, M. Tian and A. C. Chen, *J. Phys. Chem. A*, 2009, **113**, 9348; (d) G. Aromi, L. A. Barrios, O. Roubeau and P. Gamez, *Coord. Chem. Rev.*, 2011, **255**, 485; (e) J.-P. Zhang, Y.-B. Zhang, J.-B. Lin and X.-M. Chen, *Chem. Rev.*, 2012, **112**, 1001.
- (a) M. P. Placidi, A. J. L. Villaraza, L. S. Natrajan, D. Sykes, A. M. Kenwright and S. Faulkner, *J. Am. Chem. Soc.*, 2009, **131**, 9916; (b) H. Nishihara, *Coord. Chem. Rev.*, 2005, **249**, 1468.
- (a) Y.-C. Li, C. Qi, S.-H. Li, H.-J. Zhang, C.-H. Sun, Y.-Z. Yu and S.-P. Pang, *J. Am. Chem. Soc.*, 2010, **132**, 12172; (b) T. M. Klapötke and D. G. Piercey, *Inorg. Chem.*, 2011, **50**, 2732; (c) J.-M. Lin, W.-B. Chen, X.-M. Lin, A.-H. Lin, C.-Y. Ma, W. Dong and C.-E. Tian, *Chem. Commun.*, 2011, **47**, 2402.
- J.-M. Lin, M. Yang, Y.-X. Qiu, W.-B. Chen, H. Yan, F.-X. Gao, Z.-J. OuYang, W. Dong and T.-C. Kuang, *ChemPlusChem*, 2013, **78**, 598.
- T. Lu and F. Chen, *J. Comput. Chem.*, 2012, **33**, 580, <http://multiwfn.codeplex.com>.
- I. L. Shegal, K. V. Stanovkina, N. G. Kovalenko and L. M. Shegal, *Khim. Geterotsikl. Soedin*, 1974, **3**, 422.
- M. L. Kahn, J.-P. Sutter, S. Golhen, P. Guionneau, L. Ouahab, O. Kahn and D. Chasseau, *J. Am. Chem. Soc.*, 2000, **122**, 3413.
- (a) L. Sorace, C. Benelli and D. Gatteschi, *Chem. Soc. Rev.*, 2011, **40**, 3092; (b) Y.-N. Guo, X.-H. Chen, S. Xue and J.-K. Tang, *Inorg. Chem.*, 2011, **50**, 9705; (c) V. Chandrasekhar, P. Bag, M. Speldrich, J. V. Leusen and P. Kögerler, *Inorg. Chem.*, 2013, **52**, 5035; (d) G. F. Xu, Q. L. Wang, P. Gamez, Y. Ma, R. Clérac, J. K. Tang, S. P. Yan, P. Cheng and D. Z. Liao, *Chem. Commun.*, 2010, **46**, 1506; (e) M. A. Aldamen, S. Cardona-Serra, J. M. Clemente-Juan, E. Coronado, A. Gaita-Ariño, C. Martí-Gastaldo, F. Luis and O. Montero, *Inorg. Chem.*, 2009, **48**, 3467.
- (a) P.-H. Lin, T. J. Burchell, R. Clerac and M. Murugesu, *Angew. Chem., Int. Ed.*, 2008, **47**, 8848; (b) P.-H. Lin, W.-B. Sun, M.-F. Yu, G.-M. Li, P.-F. Yan and M. Murugesu, *Chem. Commun.*, 2011, **47**, 10993.
- J. Bartolome, G. Filoti, V. Kuncser, G. Schinteie, V. Mereacre, C. E. Anson, A. K. Powell, D. Prodius and C. Turta, *Phys. Rev. B: Condens. Matter*, 2009, **80**, 014430.
- (a) M. R. Saber and K. R. Dunbar, *Chem. Commun.*, 2014, **50**, 2177; (b) Y.-M. Song, F. Luo, M.-B. Luo, Z.-W. Liao, G.-M. Sun, X.-Z. Tian, Y. Zhu, Z.-J. Yuan, S.-J. Liu, W.-Y. Xu and X.-F. Feng, *Chem. Commun.*, 2012, **48**, 1006; (c) D.-P. Li,

X.-P. Zhang, T.-W. Wang, B.-B. Ma, C.-H. Li, Y.-Z. Li and X.-Z. You, *Chem. Commun.*, 2011, **47**, 6867; (d) H. Wang, C. Liu, T. Liu, S. Zeng, W. Cao, Q. Ma, C. Duan, J. Dou and J. Jiang, *Dalton Trans.*, 2013, **42**, 15355; (e) R. J. Blagg, C. A. Muryn, E. J. L. McInnes, F. Tuna and

R. E. P. Winpenny, *Angew. Chem., Int. Ed.*, 2011, **50**, 6530; (f) S.-D. Jiang, B.-W. Wang, G. Su, Z.-M. Wang and S. Gao, *Angew. Chem.*, 2010, **122**, 7610; (g) R. A. Layfield, J. J. W. McDouall, S. A. Sulway, F. Tuna, D. Collison and R. E. P. Winpenny, *Chem. - Eur. J.*, 2010, **16**, 4442.